

## Trace polarizability spectra from Ar<sub>2</sub> quasimolecules in collision-induced scattering

Omar Gaye, Michael Chrysos,\* Victor Teboul, and Yves Le Duff

*Laboratoire des Propriétés Optiques des Matériaux et Applications, CNRS EP 130, Université d'Angers,  
2 Boulevard Lavoisier, 49045, Angers, Cedex, France*

(Received 9 December 1996)

The experimental Ar<sub>2</sub> trace-polarizability collision-induced scattering spectrum is reported in absolute units and over a large range of Raman frequency shifts, up to  $\nu \approx 400 \text{ cm}^{-1}$ . At frequency shifts above  $60 \text{ cm}^{-1}$ , the measured spectral profile falls off exponentially. We were able to record the far wing down to intensities that are two orders of magnitude smaller than those of the previous work. While the long ago predicted insufficiency of the dipole-induced dipole (DID) or DID-like trace models is confirmed, reliable fully quantum computations based on a modern approach show that the *ab initio* Dacre's trace [P. D. Dacre, *Mol. Phys.* **45**, 1 (1982)] accounts well for the frequency dependence of the experimental spectrum differing only by a scaling constant. [S1050-2947(97)05905-2]

PACS number(s): 32.70.-n, 32.80.Ys, 33.20.Fb, 33.70.-w

### I. INTRODUCTION

Depending on the interatomic forces, the polarizability of a cluster of inert atoms is a key element for both the qualitative and the quantitative understanding of several macroscopic properties of a dense fluid (second- and higher-order virial coefficients of the dielectric constant, refractivity, and optical Kerr constant). Providing that the sample remains non-reactive in the encounter during the process, scattering spectra are the fingerprints of the interaction-induced variations of the cluster polarizability manifesting themselves by non-violent interatomic collisions [1,2]. At sufficiently low densities only binary interactions are physically relevant. These interactions make the polarizability of the "cluster" differ from the sum of the *permanent* polarizabilities of the two separated atoms for at least two reasons: (i) because of the fluctuating local field of a neighboring atom differing from the external field of the light source; (ii) because of short-range exchange effects and dispersion forces deforming the electronic distribution of any single atom and affecting its "permanent" polarizability [3,4].

The so-created *induced* polarizability is a function of the interparticle distance  $r$ . Its tensor is characterized by two invariants commonly known as the *trace* and the *anisotropy*, both of which depend on  $r$  and may induce scattered intensities with specific light polarizations. As concerns their mechanism, binary collision-induced light scattering (CILS) spectra from atomic systems can be seen as analogs of the familiar rotovibrational Raman spectra from diatomic molecules. It should be noted that also absorption processes experience a similar parallelism, where binary collision-induced absorption spectra can be seen as the counterparts of common rotovibrational infrared spectra from diatomic molecules [5]. Especially for gaseous argon, experimental and theoretical evidence from binary scattering spectra has to date been provided in a plethora of papers [6–11] (for representative works from different groups, see Refs. [6–10]; a

complete bibliography reviewing CILS studies up to 1989 can be found in Ref. [11]). Nevertheless, as yet this literature has almost been monopolized by investigations on depolarized spectra (often also known as anisotropic spectra) in the vicinity of the Rayleigh line. After a straightforward comparison of the experimental depolarized spectra [6,7,12], with those obtained theoretically by means of either classical or semiclassical [12–14] or fully quantum approaches [3,10,15,16], we are strengthened in our conviction that satisfactory, physically meaningful anisotropy schemes do exist [17], that they are able to reproduce within a reasonable accuracy the spectrum at least up to  $400 \text{ cm}^{-1}$  [10], i.e., the upper bound of the as yet available experimental data [12]. Besides, as regards trace spectra (often called isotropic), much less work has been done and experimental results are scarce. With this regard, Frommhold and Proffitt were the only ones to record, for the longest time, the weak isotropic signal from gaseous Ar<sub>2</sub> [18]. In that experiment, pioneering for its time, the explored frequency range was limited to  $230 \text{ cm}^{-1}$ . In comparison with theory [18,19], they concluded that no existing *ab initio* polarizability model is able to satisfactorily reproduce their spectrum. An empirical trace fitting the experiment was, however, proposed therein whose physical meaning as yet remains questionable.

Here we report experimental data in absolute units on the Ar<sub>2</sub> collision-induced scattering spectrum at room temperature. The present work is a confirmation of the only previously reported observation of collision-induced trace scattering and, at the same time, an extension of the previous work [18]. A large frequency range extended up to  $\nu \approx 400 \text{ cm}^{-1}$  is probed. Intensities weaker than the ones previously measured by more than two orders of magnitude are recorded. A complete and systematic quantum analysis of the light scattering intensities is performed for the same frequency range and several trace models are checked and compared with the experiment. From this analysis, a new semiempirical trace model is obtained that permits the computational reproduction of the measured trace spectra.

The paper is organized as follows: In Sec. II the conditions of the experiment are briefly described and the details

\*Author to whom correspondence should be addressed.

in collecting the isotropic intensities are stressed. In Sec. III the theoretical method for calculating the spectrum is briefly given, together with the computational implementation. Results are presented and discussed in Sec. IV. Concluding remarks are given in Sec. V.

## II. EXPERIMENT

The isotropic collision-induced scattering intensities of argon are measured by making use of an experimental setup previously described within the study of the depolarized light scattering [12]. We use the green line ( $\lambda = 514.5$  nm) of a 2.5-W argon-ion laser. The gaseous argon is provided by the L'Air Liquide Company with residual impurities of about 1 ppm. The sample is contained in a high-pressure four-window cell and stabilized at a temperature  $T = 294.5 \pm 0.5$  K. Argon densities are deduced from pressures measured within an accuracy of 1% and using physical vapor transport (PVT) data from Ref. [20]. To obtain isotropic scattering spectra two types of intensities were collected, namely,  $I_H$  and  $I_V$ , corresponding to the light scattered by the gaseous sample with the laser polarization, respectively, parallel and perpendicular to the scattering plane [21]. Rotation of the polarization vector of the laser beam is possible by using a half-wave plate associated with a glan prism. For each Raman shift  $\nu$ ,  $I_H(\nu)$ , and  $I_V(\nu)$  may be written as functions of the isotropic  $I_{\text{ISO}}(\nu)$  and of the depolarized (anisotropic)  $I_{\parallel}(\nu)$  components, following the equations [8,22]:

$$I_H(\nu) = aI_{\text{ISO}}(\nu) + dI_{\parallel}(\nu), \quad (1)$$

$$I_V(\nu) = cI_{\text{ISO}}(\nu) + bI_{\parallel}(\nu), \quad (2)$$

where  $a$ ,  $b$ ,  $c$ , and  $d$  are coefficients depending on the collection angle  $\theta_c$  of the scattering beam. For the limiting value  $\theta_c = 0$  one obtains  $a = 0$ ,  $b = \frac{7}{6}$ , and  $c = d = 1$ . When defining the depolarization ratio by  $\eta_n(\nu) = I_H(\nu)/I_V(\nu)$ , Eqs. (1) and (2) provide

$$I_{\text{ISO}}(\nu) = \frac{d - b\eta_n(\nu)}{c\eta_n(\nu) - a} I_{\parallel}(\nu). \quad (3)$$

In our experimental setup the scattering angle was chosen  $\theta_c = 6.2^\circ$ . Whatever the frequency  $\nu$ , this choice gives rise to the condition  $a \ll c\eta_n$ , establishing the following expression for the trace spectrum:

$$I_{\text{ISO}}(\nu) = \left\{ \frac{1.004}{\eta_n(\nu)} - 1.1695 \right\} I_{\parallel}(\nu). \quad (4)$$

From this equation, the values of the isotropic intensities in absolute units are deduced directly from the corresponding intensities for the anisotropic spectrum  $I_{\parallel}(\nu)$  measured previously, also in absolute units [12]. Consequently, the accuracy of the collected data on isotropic intensities depends on that of the  $I_{\parallel}(\nu)$  and  $\eta_n(\nu)$  measurements. In the particular case of probing low-frequency shift regions, collision-induced scattering is almost completely depolarized, described by a depolarization ratio of the value  $\frac{6}{7}$  as  $\nu$  approaches the unshifted Rayleigh line. As a consequence, difficulties will appear in the precise measurement of the difference  $\eta_n(\nu) - \frac{6}{7}$ , i.e., the numerator of Eq. (4); this ex-

TABLE I. Experimental intensities (in  $\text{cm}^6$ ) of the isotropic Ar<sub>2</sub> scattering spectrum at  $T = 295$  K, as a function of  $\nu$  (in  $\text{cm}^{-1}$ ) in the interval  $60 \leq \nu \leq 400 \text{ cm}^{-1}$ . A drastic attenuation of the isotropic intensity is found with increasing  $\nu$ , corresponding to five orders of magnitude between  $\nu = 60 \text{ cm}^{-1}$  and  $\nu = 400 \text{ cm}^{-1}$ . Intensities in parentheses denote estimated experimental values.

$\nu$ ( $\text{cm}^{-1}$ )	$I_{\text{ISO}}$ ( $\text{cm}^6$ )	$\nu$ ( $\text{cm}^{-1}$ )	$I_{\text{ISO}}$ ( $\text{cm}^6$ )
60	$(1.13 \times 10^{-56})$	220	$8.85 \times 10^{-59}$
65	$1.34 \times 10^{-56}$	230	$6.44 \times 10^{-59}$
70	$1.61 \times 10^{-56}$	240	$4.71 \times 10^{-59}$
75	$5.00 \times 10^{-57}$	250	$3.22 \times 10^{-59}$
80	$8.89 \times 10^{-57}$	260	$2.51 \times 10^{-59}$
85	$6.24 \times 10^{-57}$	270	$1.66 \times 10^{-59}$
90	$4.30 \times 10^{-57}$	280	$1.25 \times 10^{-59}$
100	$3.89 \times 10^{-57}$	290	$9.62 \times 10^{-60}$
110	$3.26 \times 10^{-57}$	300	$6.76 \times 10^{-60}$
120	$2.45 \times 10^{-57}$	310	$4.94 \times 10^{-60}$
130	$1.62 \times 10^{-57}$	320	$3.64 \times 10^{-60}$
140	$1.11 \times 10^{-57}$	330	$2.70 \times 10^{-60}$
150	$7.52 \times 10^{-58}$	340	$1.76 \times 10^{-60}$
160	$6.40 \times 10^{-58}$	350	$1.60 \times 10^{-60}$
170	$3.99 \times 10^{-58}$	360	$1.06 \times 10^{-60}$
180	$3.04 \times 10^{-58}$	370	$8.42 \times 10^{-61}$
190	$2.25 \times 10^{-58}$	380	$7.15 \times 10^{-61}$
200	$1.67 \times 10^{-58}$	390	$(4.47 \times 10^{-61})$
210	$1.14 \times 10^{-58}$	400	$(2.59 \times 10^{-61})$

plains why  $I_{\text{ISO}}$  for the low-frequency domain  $\nu \leq 60 \text{ cm}^{-1}$  is measured within a poor accuracy and is not given in Table I. However, estimations of the experimental intensities in this frequency domain can be made and are given in Fig. 1. Our spectra are obtained up to  $400 \text{ cm}^{-1}$  using large slit widths varying from  $4 - 8 \text{ cm}^{-1}$  according to the frequency probed. Each measurement is further corrected in order to take into account the wavelength dependence of the spectral sensitivity of our apparatus (double monochromator and photomultiplier).

## III. THEORY AND COMPUTATIONS

In order to perform an accurate quantum analysis of the Ar<sub>2</sub> system, a modern methodology is applied as described in Refs. [10,16]. This methodology allows for the systematic computation of frequency-resolved and -integrated Rayleigh and Raman spectra from stable, metastable, and free Ar dimers over a large band of frequencies, and is based on a suitable combination of an analytical discrete variable representation (DVR) [23,24] coupled to a propagative (Fox-Goodwin) [25,26] integrator. This DVR consists in a simple numerical procedure that can be programmed in a few lines, where the matrix elements of the potential operator are diagonal while those of the kinetic energy operator are analytically known [27]. It is noteworthy that, by means of this implicit basis-set method, discretization of the low-energy continuum (lf) becomes possible as well [16]. When transitions between bound ( $b$ ), metastable ( $m$ ), or low-energy free (lf) states of the quasimolecule are involved, the DVR provides an efficient means to systematically compute accurate

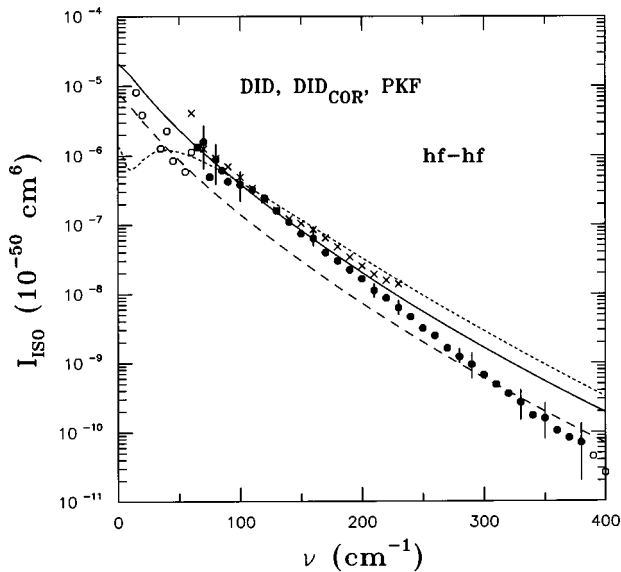


FIG. 1. Trace (isotropic) intensities ( $I_{\text{ISO}}$ ) of  $\text{Ar}_2$  collision-induced scattering spectra (in  $\text{cm}^6$ ) at  $T=295$  K versus frequency (in  $\text{cm}^{-1}$ ), illustrated in semilogarithmic scale. Filled circles stand for our experimental measurements where uncertainties are indicated by error bars; open circles represent estimated experimental intensities in the extremities of the frequency domain probed. The form of the spectrum seems to reveal a purely exponential frequency law. Crosses denote measurements from the previous experimental work [34]. Curves stand for the different trace models:  $\text{DID}_{\text{COR}}$  (solid curve), DID (long-dashed curve), and PKF (short-dashed curve). The slope of DID and  $\text{DID}_{\text{COR}}$  trace models (in semilogarithmic scale) differs from that of the experiment. Beyond  $60 \text{ cm}^{-1}$  the spectrum is practically purely rototranslational.

eigenenergies and wave functions; propagative techniques, so far monopolizing collision-induced studies, can give rise to instabilities due to the (in principle) unguided choice of the initializing energies in a multidiscrete-level quantized system. In addition, when mean potentials (effective one-dimensional potentials describing many-body interactions) are treated, usually extracted from radial distribution functions with structure, it turns out that ordinary propagative techniques and matching procedures are particularly inadequate due to the multitude of successive classically forbidden and allowed regions of the potential. On the other hand, transitions involving high-energy free states (hf) of the dimer can be handled safely only by a propagative approach, set up within a mixed procedure. In this work the two-point Fox-Goodwin algorithm (coupled to the DVR) is used, building up the ratio of the wave function at adjacent grid points. Note, in passing, that apart from its simplicity and stability, this integrator can be extended to a  $N \times N$  matrix form to solve the much more complicated multichannel problem (where more than one physically relevant potential surfaces are coupled to each other by either interatomic, intramolecular, or radiative fields) even when the interaction persists at infinity [28].

As regards our problem, trace spectra are computed by using the following equation [29]:

$$I_{\text{ISO}}(\nu) = hck_0(\kappa L)^3 \sum_{J \text{ even}}^{J_c} (2J+1) \sum_m \int e^{-E_m/kT} \times \sum_n |\langle \psi_{n,J} | \Delta\alpha | \psi_{m,J} \rangle|^2 \delta\epsilon_m \delta\epsilon_n \delta(E_n - E_m - h\nu), \quad (5)$$

$\Delta\alpha$  denoting the incremental trace function of the dimer. Discrete summations in Eq. (5) are over bound or sharp-resonance states where index  $m$  ( $n$ ) characterizes the initial (final) state with energy  $E_{m(n)}$ ; for all transitions departing (arriving) from (at) sharp resonances or bound states it is  $\delta\epsilon_{m(n)} = 1$ . For transitions departing (arriving) from (at) broad resonances or pure scattering states embedded in the lf continuum (for which the DVR discretization procedure still accounts well), it is  $\delta\epsilon_{m(n)} = E_{m(n)+1} - E_{m(n)}$ . Finally, for transitions departing (arriving) from (at) hf states, normal integration should be made and  $\delta\epsilon_{m(n)} \rightarrow dE$ , the latter being approximated by a constant integration step  $\Delta E$ ; it is noteworthy that  $\Delta E$  can be given a relatively large value ( $10\text{--}20 \text{ cm}^{-1}$ ) to accelerate computations. For values of  $J$  creating a three-turning point effective interaction potential ( $V_{\text{eff}}^J$ ), the lower bound in the integral should be chosen as the barrier top of  $V_{\text{eff}}^J$ .  $\psi_{m(n),J}$  denotes wave function of a level with energy  $E_{m(n)}$  (discrete or not) with the same rotational quantum number  $J$  for both the initial and final states. Constant  $L$  stands for the de Broglie wavelength,  $L = h/\sqrt{2\pi\mu kT}$ ;  $k$  is the Boltzmann constant;  $\kappa$  stands for the wave number of the scattered wave and  $k_0$  for the laser wave number,  $k_0 = 2\pi/\lambda_L$ ; with  $\lambda_L = 5145 \text{ \AA}$  the laser wavelength at the green spectral line of argon. When hf states are involved, the  $\delta$  function drops one of the two integrals, but in all other cases (involving discrete summations) it should be substituted by an, as realistic as possible, instrumental slit function convoluting the spectrum. Here a triangular function of unit area (denoted by  $\Lambda$  in distribution theory) is used, deriving from the convolution ( $\Lambda = \Pi * \Pi$ ) of two identical (spectrometer) slits, each represented by an ideal rectangular function of unit area (denoted by  $\Pi$ ); the width of the  $\Lambda(\nu)$  function at half maximum is chosen to be  $4 \text{ cm}^{-1}$  to simulate experimental conditions (see Sec. II). The coupling function  $\Delta\alpha(r)$  stands for the trace of the polarizability tensor of the quasimolecule. Here, four trace models are checked.

(i) The two-term dipole-induced dipole model (DID) [3,30]:

$$\Delta\alpha(r) = \frac{4\alpha_0^3}{r^6} + \frac{4\alpha_0^4}{r^9}, \quad (6)$$

where  $\alpha_0 = 11.337a_0^3$  stands for the dynamic polarizability of the argon atom at the green argon laser wavelength, and  $a_0$  for the Bohr radius.

(ii) The corrected DID trace ( $\text{DID}_{\text{COR}}$ ), attempting to analytically model the London dispersion effects in terms of the hyperpolarizability  $\gamma$  and the (positive) van der Waals coefficient  $C_6$  [31]. This correction has an impact already on the first nonzero term of the DID expansion, which now reads

$$\Delta\alpha(r) = \left\{ 4\alpha_0^3 + \frac{5\gamma C_6}{9\alpha_0} \right\} \frac{1}{r^6} + \dots = \frac{A_6}{r^6} + \dots, \quad (7)$$

where  $A_6 = 9665a_0^9$ .

(iii) The empirical Proffitt-Keto-Frommhold (PKF) model, fitting their experimental trace spectrum (see Sec. I) [8]:

$$\Delta\alpha(r) = \frac{A_6}{r^6} - t_0 \exp\left[-\frac{r-\sigma}{R_t}\right], \quad (8)$$

where the values of the parameters have been determined as  $t_0 = 0.214a_0^3$ ,  $\sigma = 6.34a_0$ , and  $R_t = 0.764a_0$ .

(iv) The *ab initio* self-consistent field (SCF) model of Dacre [17], properly taking into account the (short-range) overlap and exchange phenomena but neglecting any electronic correlation. Given that this model was not obtained with the inclusion of configuration interaction (which is known to be essential for such work), Dacre's results are certainly not the last word on the topic; however, it is true that they are still the most advanced in existence.

Dacre's computations were based to some extent on empirical scaling factors; very substantial counterpoise corrections were required. The SCF trace used here contains the counterpoise corrections and is taken in numerical form from Ref. [17] [see (column 6) Table 4 therein]. Given that overlap and exchange effects become insignificant at large interparticle separations, the SCF trace has to join the DID model asymptotically; however the resulting asymptotic model differs from the expected DID one by a scaling constant, as if the Ar polarizability were given the fictitious value  $\alpha_{\text{SCF}} = 10.384a_0^3$ . To remove this inconsistency, scaling of the SCF trace function has been proposed by the constant  $(\alpha_0/\alpha_{\text{SCF}})^3$ . This operation gives rise to a new model, the so-called corrected SCF (SCF<sub>COR</sub>) [19].

As regards the DVR part of our mixed algorithm, a box extended to interatomic distance  $l = 60$  bohr is used and various grids are checked ranging from  $N = 150$ –400 points. Reported results have converged within  $<1\%$  for all transitions. The analytical Hamiltonian matrix is repeatedly diagonalized for all even values of  $J$  in the interval  $0 \leq J \leq J_c$  with  $J_c = 58$ . Only in this interval can bound, shape-resonance, and low-energy scattering states be accommodated, given that the effective potential presents a three-turning point topology there [16]. Only the eigenvalues of the Hamiltonian matrix lying below the barrier top  $E_c^J$  are retained for each value of  $J$ . Among those eigenvalues, negative energies correspond to bound states and therefore to stable dimers. Positive energies, on the other hand, correspond to the continuum, which is embedded in the two potential wells formed by  $V_{\text{eff}}^J$  and the right edge of the box (discretization of the continuum). The latter eigenvalues account for (i) sharp resonances, associated with predissociating (metastable) dimers and (ii) low-energy pure scattering states and broad resonances, associated with low-energy free Ar-Ar quasimolecules. The nature of each of the positive energy states is distinguished by means of a simple technique described in Ref. [16].

For quantum numbers  $J > J_c$  only hf states exist, for which the DVR alone is inappropriate. The Fox-Goodwin outward propagator of our mixed procedure is then automatically activated. Numerical parameters are chosen as in the previous studies for the anisotropic spectrum [10]; namely, a spatial grid extended from 3 to 150 bohr with a grid step of

0.35 bohr; the upper bound in the integral over energy is chosen to be  $3000 \text{ cm}^{-1}$ , and the corresponding integration step  $\Delta E = 10 \text{ cm}^{-1}$ ; the maximum angular-momentum quantum number is taken 700, where all  $J$  are computed in the interval 0–100, while, for  $J > 100$ , matrix elements are calculated only every ten values of  $J$  and then interpolated to give intermediate values. The response of this procedure was carefully checked and compared with the full computation, providing an excellent accuracy within  $<0.05\%$  for any  $\nu$  but accelerating computations by a factor  $>7$ . The trace spectra are then computed by using Eq. (5) and following the same methodology as for the depolarized ones (for more details, see Refs. [10,16]). In view of the large experimental uncertainties (several tens of %), the computed intensities are obtained by optimizing all numerical parameters, aiming at a good compromise between comparative accuracy versus numerical economy. In this way, the overall numerical error relative to the computed intensities is evaluated between 1.5% and 5%, depending on the frequency region, while that on the zeroth-order moment is estimated to about 3%. The Aziz-Slaman potential [32] is used for all computations, corresponding to one of the best Ar-Ar interactions ever proposed. Finally, cubic  $B$  splines [33] are applied to both potential and numerical trace models to convert them to piecewise analytic functions.

#### IV. RESULTS

Table I shows the experimental trace intensities,  $I_{\text{ISO}}$  (in  $\text{cm}^6$ ), as a function of  $\nu$ . For  $\nu > 100 \text{ cm}^{-1}$  the intensities deviate progressively from those illustrated in the previous experimental work [8] (and that are also shown graphically in Fig. 1 [34]). Table II confronts experiment with theory for representative values of  $\nu$  and for both the DID and SCF trace functions [see Sec. III, models (i) and (iv)]. The ratio between experimental and theoretical intensities is also given for both models. In the case of the (classical) DID, this ratio gradually decreases with increasing  $\nu$ , while that referring to the *ab initio* SCF trace remains quasicontant throughout the entire ( $70 \leq \nu \leq 380 \text{ cm}^{-1}$ ) frequency domain. Figure 1 illustrates experimental intensities from our group (circles), together with those of the previous experiment (crosses) [34] (for error bars referring to this latter experiment, we address the reader to Ref. [18]), compared with our calculated spectra (lines) for both the DID and DID<sub>COR</sub> models. Experimental error bars are also shown on our data. As one sees, experimental measurements present high uncertainties ( $>50\%$ ) for frequencies  $\leq 80 \text{ cm}^{-1}$  and  $\geq 350 \text{ cm}^{-1}$ . The first type of uncertainties, at low frequencies, comes from the fact that depolarization ratios approach their maximum value ( $\frac{6}{7}$ ) as  $\nu \rightarrow 0$ , while the second one, at high frequencies, simply comes from the absolute feebleness of the detected signal. Since bound or predissociative states do not perturb the spectrum beyond  $60 \text{ cm}^{-1}$  (where experimental data are given within a reasonable accuracy), the difference between  $I_{\text{ISO}}$ , and its high-energy rototranslational hf-hf component becomes practically indiscernible. For  $\nu \leq 60 \text{ cm}^{-1}$  (where experimental measurements present uncertainties exceeding 100%), experimental intensities are meaningless; estimations of their values are however indicated and are represented by open circles. As Fig. 1 suggests, at intermediate frequencies

TABLE II. Comparison between experimental and theoretical spectra (in  $\text{cm}^6$ ) for representative values of  $\nu$  (in  $\text{cm}^{-1}$ ). Two trace functions are examined: the (classical) DID model and the (quantum) SCF one. For both models the ratio experiment: theory is also given. The insufficiency of the DID to describe the entire frequency interval is clearly seen. For the SCF trace, the almost constant ratio shows that, surprisingly, the frequency dependence of the experimental spectrum is well reproduced.

$\nu$ ( $\text{cm}^{-1}$ )	Experiment	DID ( $\text{cm}^5$ )	Experiment: Theory	SCF ( $\text{cm}^6$ )	Experiment: Theory
80	$8.89 \times 10^{-57}$	$2.80 \times 10^{-57}$	3.2	$1.07 \times 10^{-56}$	0.8
100	$3.89 \times 10^{-57}$	$1.42 \times 10^{-57}$	2.7	$6.04 \times 10^{-57}$	0.6
120	$2.45 \times 10^{-57}$	$7.46 \times 10^{-58}$	3.3	$3.24 \times 10^{-57}$	0.7
160	$6.40 \times 10^{-58}$	$2.24 \times 10^{-58}$	2.9	$8.73 \times 10^{-58}$	0.7
200	$1.67 \times 10^{-58}$	$7.36 \times 10^{-59}$	2.3	$2.34 \times 10^{-58}$	0.7
220	$8.85 \times 10^{-59}$	$4.34 \times 10^{-59}$	2.0	$1.22 \times 10^{-58}$	0.7
240	$4.71 \times 10^{-59}$	$2.59 \times 10^{-59}$	1.8	$6.39 \times 10^{-59}$	0.7
280	$1.25 \times 10^{-59}$	$9.68 \times 10^{-60}$	1.3	$1.81 \times 10^{-59}$	0.7
300	$6.76 \times 10^{-60}$	$6.04 \times 10^{-60}$	1.1	$9.74 \times 10^{-60}$	0.7
340	$1.76 \times 10^{-60}$	$2.45 \times 10^{-60}$	0.7	$2.91 \times 10^{-60}$	0.6
360	$1.06 \times 10^{-60}$	$1.59 \times 10^{-60}$	0.7	$1.60 \times 10^{-60}$	0.7
380	$7.15 \times 10^{-61}$	$1.05 \times 10^{-60}$	0.7	$8.89 \times 10^{-61}$	0.8

( $70 \leq \nu \leq 200 \text{ cm}^{-1}$ ),  $\text{DID}_{\text{COR}}$  reproduces well the experimental spectrum becoming insufficient in the far wings. The asymptotic DID trace, on the other hand, displaying (in semilogarithmic scale) the same slope as that of the  $\text{DID}_{\text{COR}}$  model, joins the experimental spectrum from below. Both DID and  $\text{DID}_{\text{COR}}$ , however, are unable to describe the entire frequency interval probed. In the same figure, the PKF model [see Sec. III, model (iii)] is shown as well. From comparison with our measurements we conclude that the response of the PKF model for this set of parameters is not satisfactory. This finding should be expected since the PKF model has been conceived (and its parameters have been adjusted) to fit the

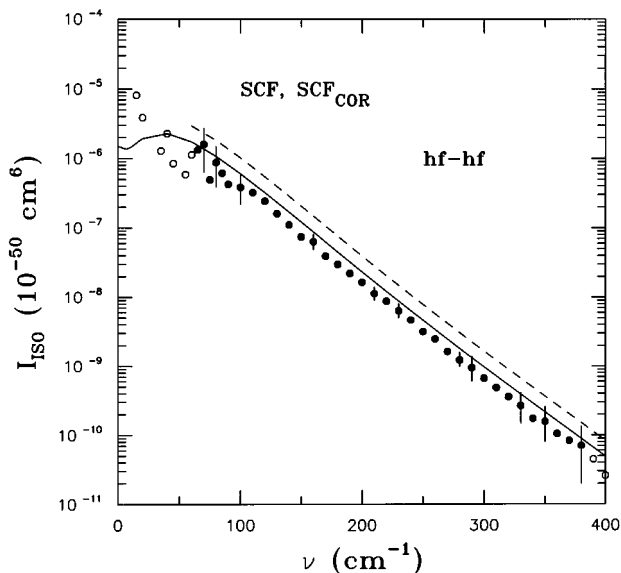


FIG. 2. Same as in Fig. 1, but for the SCF (solid curve) and  $\text{SCF}_{\text{COR}}$  (dashed curve) trace functions. The slope of the experiment (in semilogarithmic scale) is perfectly reproduced by both models. This finding enables one to conceive an optimal model (at least for  $\nu > 60 \text{ cm}^{-1}$  where measurements are sufficiently accurate) differing by the Dacre's trace by a scaling constant.

older experimental spectrum (restricted to a much smaller frequency domain) [8] whose intensities are clearly different from ours beyond  $100 \text{ cm}^{-1}$  in the common  $\nu$  domain.

In Fig. 2 the experimental data are again shown in comparison with the *ab initio* Dacre's trace functions [see Sec. III, model (iv)]. Since these functions differ by a constant, they again both exhibit the same slope in semilogarithmic scale. However, to our pleasant surprise, these models are seen to remarkably reproduce the slope of the experimental spectrum (in semilogarithmic scale) all along the  $\nu$  interval where experimental data are meaningful. This observation suggests a new model resulting from the Dacre's SCF trace by simply a scaling constant. The value of this constant is estimated to about  $\sqrt{0.7} \approx 0.85$ , as one deduces from Table II. Its physical meaning, although still unclear, should be searched in the notion of a global negative contribution to the induced polarizability trace that will no longer converge to the ordinary DID asymptotically.

In Fig. 3 the contribution of the stable and predissociating  $\text{Ar}_2$  dimers ( $b, m$ ) is illustrated as an example for the  $\text{DID}_{\text{COR}}$  trace. The contribution of the free  $\text{Ar}_2$  dimers corresponding to the continuum with energies below that of the potential barrier (lf) (discretization of the continuum) is shown there, as well. All these transitions have impact only on a limited  $\nu$  range as is also the case for the depolarized spectrum. Transitions involving stable and predissociating dimers give clearly rise to two lobes, respectively, peaking at  $\nu \approx \pm 18 \text{ cm}^{-1}$  of the Stokes and anti-Stokes spectral sides. In the vicinity of the origin a steep peak is found, corresponding to the unshifted Rayleigh response of the  $\text{Ar}_2$  molecule. Attempting to simulate as closely as possible the experimental conditions, a  $\Lambda$  instrumental slit of width at half maximum equal to  $4 \text{ cm}^{-1}$  is used, giving rise to a Rayleigh peak of triangular form centered at  $\nu = 0$  and settling down beyond  $\pm 4 \text{ cm}^{-1}$  (see Fig. 3). This peak (where all three types of direct transitions, i.e.,  $b$ - $b$ ,  $m$ - $m$ , and lf-lf, have their absolute maximum) goes up to values exceeding 50 times those of the lobe maxima.

As regards integrated spectra, it should be stressed that

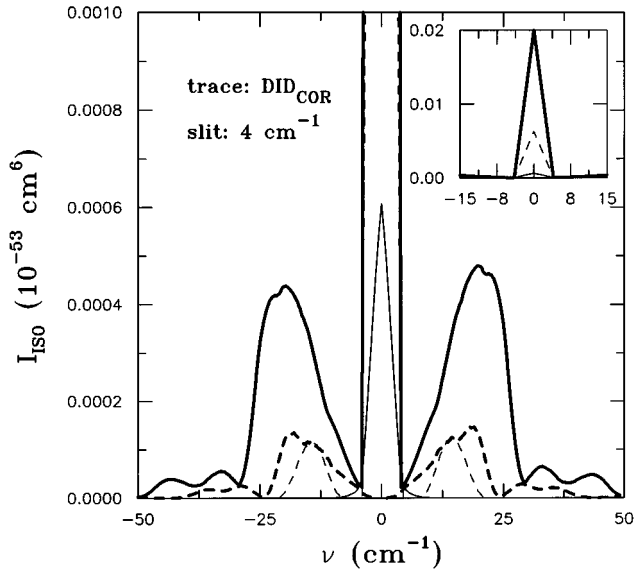


FIG. 3. Rovibrational Raman components of the trace intensities ( $I_{\text{ISO}}$ ) (in  $\text{cm}^6$ ) at  $T=295$  K versus frequency (in  $\text{cm}^{-1}$ ) for both the Stokes and anti-Stokes spectral sides in the interval  $-50 \leq \nu \leq 50 \text{ cm}^{-1}$  where rovibrational structure is very pronounced. As an example, the  $\text{DID}_{\text{COR}}$  trace model is illustrated. A triangular slit of width at half maximum equal to  $4 \text{ cm}^{-1}$  is used to simulate as closely as possible the experimental conditions in this interval. Different types of transitions are illustrated: bound to bound states ( $b$ - $b$ ) (thick solid curve); bound to predissociating states and inversely ( $b$ - $m$ ) (thick dashed curve); predissociating to predissociating states ( $m$ - $m$ ) (thin dashed curve); low-energy free to low-energy free states (lf-lf) (thin solid curve). All the three direct transitions ( $b$ - $b$ ,  $m$ - $m$ , and lf-lf) have the absolute maximum at  $\nu = 0$  giving rise to a sharp Rayleigh peak. At  $\nu \approx \pm 18 \text{ cm}^{-1}$  the rovibrational Raman lobes peak for both stable and predissociating quasimolecules. In the inset the region around  $\nu=0$  is enlarged in order to show up the sharp isotropic Rayleigh peak due to rovibrational transitions. Its intensity exceeds that of the lobe maxima, formed by the same transitions, by 50 times. This feature of the isotropic scattering spectrum should be contrasted to that for the anisotropic one.

due to the absence of accurate experimental data in the low-frequency domain ( $\nu \leq 60 \text{ cm}^{-1}$ ), moments referring to experimental intensities are highly uncertain and their comparison with the theoretical spectra has only a very limited meaning. However, a value for the zeroth-order moment ( $m_0$ ) is indicated in Table III, obtained by interpolation of the experimental data in the low-frequency part between Stokes and anti-Stokes spectral sides. For the sake of comparison, the theoretical zeroth-order moment is also computed, and is shown there for two trace models.

TABLE III. Isotropic total zeroth-order moments ( $m_0$ ) expressed in  $10^{-14} \text{ \AA}^5$ . Calculations are done by making use of both experimental and theoretical spectra for two representative trace functions, i.e., the PKF and DID models. Accuracy is within 3%. Parentheses denote estimated experimental values.

Experiment	PKF	DID
(5.8)	$1.87 \pm 0.06$	$3.47 \pm 0.10$

TABLE IV. Partial contributions to the zeroth-order moment (in  $10^{-14} \text{ \AA}^5$  and in %) from transitions involving stable ( $b$ ), predissociating ( $m$ ), and high-energy free (hf) Ar<sub>2</sub> quasimolecules. As an example, the  $\text{DID}_{\text{COR}}$  trace model is given. Stable and quasistable dimers contribute about 14% of the integrated intensity. Transitions contributing  $< 0.5\%$  to the  $m_0$  are not reported.

$m_0$	$m_{0,\text{hf-hf}}$	$m_{0,b-b}$	$m_{0,m-m}$	$m_{0,b-m}$
11.23	9.57	0.998	0.241	0.05
100 %	85.4%	11.3%	2.5%	0.5%

Finally, in Table IV the partial contributions to the zeroth-order moment from stable, predissociative, and free Ar<sub>2</sub> quasimolecules are computed, and given for the  $\text{DID}_{\text{COR}}$  model. Transitions contributing  $< 0.5\%$  to the  $m_0$  are not reported.

In order to illustrate the strong dependence of the computed spectra with the trace model checked, we calculate the second virial coefficient of the dielectric constant  $B_\epsilon$ , defined as [3]

$$B_\epsilon = \frac{8}{3} \pi^2 \mathcal{N}^2 \int_0^\infty \Delta \alpha(r) \exp\left\{-\frac{V(r)}{kT}\right\} r^2 dr, \quad (9)$$

where  $V(r)$  stands for the interaction potential and  $\mathcal{N}$  for the Avogadro's number. In Table V, the values of the  $B_\epsilon$  are given as they bear out from our computations for different trace models, and compared to experimental ones given by other groups in previous studies [8,35]. We see that the theoretical value when using the SCF trace is much smaller than those corresponding to the DID or  $\text{DID}_{\text{COR}}$  models, and than those of the experiments. The explanation for this feature comes probably from the fact that Dacre's trace acquires large negative values at short distances, thus giving rise to cancellations in the integral of Eq. (9). On physical grounds, the origin of this behavior should be searched in the fact that electronic correlation has been omitted in the *ab initio* quantum chemistry calculations. This electronic correlation is expected to add a large positive contribution to  $B_\epsilon$ .

As overall additional remarks, large deviations are marked in the computed isotropic intensities when using different trace models, confirming conclusions of previous works. When comparing with the depolarized Ar<sub>2</sub> spectrum, computed isotropic intensities are by far more sensitive to the choice of the trace than what depolarized spectra are for different anisotropy models. The isotropic intensities are much weaker than those of the anisotropic spectrum, giving rise to zeroth-order moments smaller than the anisotropic ones by at least two orders of magnitude. The percent contribution of the stable, predissociating and free Ar<sub>2</sub> quasi-

TABLE V. Second virial coefficient of the dielectric constant  $B_\epsilon$  at 322 K, expressed in  $\text{cm}^6 \text{ mol}^{-2}$ . Results are reported by making use of the DID,  $\text{DID}_{\text{COR}}$ , and SCF trace models. Comparison is made with two experimental results from other groups.

Experiment		Theory		
Ref. [8]	Ref. [35]	DID	$\text{DID}_{\text{COR}}$	SCF
0.73	$1.76 \pm 0.05$	2.37	3.82	0.040

molecules to the integrated trace intensities are generally comparable to those for the anisotropic spectrum. However, in the case of the isotropic spectrum and for all models checked, stable and predissociating dimers populate a larger frequency domain ( $-50 \leq \nu \leq 50 \text{ cm}^{-1}$ ) than that of the anisotropic spectrum ( $-10 \leq \nu \leq 10 \text{ cm}^{-1}$ ) [16]. In addition, the ratio of the rovibrational Rayleigh peak over the intensity of the corresponding rototranslational background around  $\nu = 0$  is much more pronounced for the isotropic spectrum than for the anisotropic one for the same slit function. In order to explain the cause of this pronounced Rayleigh peak as compared to the Raman structure, we recall that, in contrast to the anisotropic spectrum where selection rules are  $\Delta J = 0, \pm 2$ , in isotropic scattering only transitions conserving angular momentum ( $\Delta J = 0$ ) are allowed.

## V. CONCLUSION

The extremely weak  $\text{Ar}_2$  trace spectrum was measured with an incomparable accuracy and over a large frequency domain extended up to  $\nu \approx 400 \text{ cm}^{-1}$ . This interval exceeds by far that a previous experimental study, which was so far the only experimental evidence available in the literature.

The information coming from our measurements revealed spectral intensities that diminish exponentially with frequency (at least for  $\nu > 60 \text{ cm}^{-1}$ ), attaining signals weaker than the smallest isotropic intensities observed so far by more than two orders of magnitude. In opposition to anisotropic spectra, where the quality of a measurement is improved with decreasing  $\nu$ , experimental measurements in trace spectra are highly uncertain also in low frequencies ( $\nu \leq 60 \text{ cm}^{-1}$ ), progressively deteriorating as  $\nu$  decreases further. In order to simulate the aforementioned spectra, the quantum theory was applied by making use of a modern systematic and reliable mixing approach. From the comparison between experiment and theory we concluded that, although no model is completely satisfactory, the SCF trace reproduces well the functional dependence of the experimental spectrum beyond  $60 \text{ cm}^{-1}$ . This remark enabled us to propose a model resulting from the SCF one by just a scaling constant ( $< 1$ ). Work thereon is in progress in our institute.

## ACKNOWLEDGMENT

We thank Professor L. Frommhold for communicating to us his experimental data on the binary argon trace intensities.

- 
- [1] J. P. McTague and G. Birnbaum, *Phys. Rev. Lett.* **21**, 661 (1968).
- [2] W. M. Gelbart, *Adv. Chem. Phys.* **26**, 1 (1974).
- [3] L. Frommhold, *Adv. Chem. Phys.* **46**, 1 (1981).
- [4] G. C. Tabisz and M. N. Neuman, in *Collision- and Interaction-Induced Spectroscopy*, Vol. C452 of *NATO Advanced Study Institute, Series C: Mathematical and Physical Sciences*, edited by G. C. Tabisz and M. N. Neuman (Kluwer, Dordrecht, 1995).
- [5] L. Frommhold, *Collision Induced Absorption in Gases* (Cambridge University Press, Cambridge, 1993).
- [6] D. P. Shelton and G. C. Tabisz, *Mol. Phys.* **40**, 285 (1980).
- [7] F. Barocchi, M. Zoppi, M. H. Proffitt, and L. Frommhold, *Can. J. Phys.* **59**, 1418 (1981).
- [8] M. H. Proffitt, J. W. Keto, and L. Frommhold, *Can. J. Phys.* **59**, 1459 (1981).
- [9] H. P. Godfried and I. F. Silvera, *Phys. Rev. Lett.* **48**, 1337 (1982).
- [10] M. Chrysos, O. Gaye, and Y. Le Duff, *J. Phys. B* **29**, 583 (1996).
- [11] A. Borysow and L. Frommhold, *Adv. Chem. Phys.* **75**, 439 (1989).
- [12] F. Chapeau-Blondeau, V. Teboul, J. Berru e, and Y. Le Duff, *Phys. Lett. A* **173**, 153 (1993).
- [13] J. I. Gersten, *Phys. Rev. A* **4**, 98 (1971).
- [14] N. Meinander, G. C. Tabisz, and M. Zoppi, *J. Chem. Phys.* **84**, 3005 (1986).
- [15] L. Frommhold, K. Hong Hong, and M. Proffitt, *Mol. Phys.* **35**, 665 (1978).
- [16] M. Chrysos, O. Gaye, and Y. Le Duff, *J. Chem. Phys.* **105**, 31 (1996).
- [17] P. D. Dacre, *Mol. Phys.* **45**, 1 (1982).
- [18] L. Frommhold and M. H. Proffitt, *J. Chem. Phys.* **74**, 1512 (1981).
- [19] P. D. Dacre and L. Frommhold, *J. Chem. Phys.* **76**, 3447 (1982).
- [20] J. H. Dymond and E. B. Smith, *The Virial Coefficient of Gases* (Clarendon, Oxford, 1969).
- [21] As scattering plane we define the plane formed by the laser beam and the axis of the scattering solid angle.
- [22] B. J. Berne and R. Pecora, *Dynamic Light Scattering* (Wiley, New York, 1976).
- [23] R. W. Heather and J. C. Light, *J. Chem. Phys.* **79**, 147 (1983).
- [24] J. C. Light, I. P. Hamilton, and J. V. Lill, *J. Chem. Phys.* **82**, 1400 (1985).
- [25] D. W. Norcross and M. J. Seaton, *J. Phys. B* **6**, 614 (1973).
- [26] B. R. Johnson, *J. Chem. Phys.* **69**, 4678 (1978).
- [27] D. T. Colbert and W. H. Miller, *J. Chem. Phys.* **96**, 82 (1992).
- [28] M. Chrysos and R. Lefebvre, *J. Phys. B* **26**, 2627 (1993).
- [29] G. Placzek, Lawrence Radiation Laboratory Report No. UCRL-Trans-526 (L), 1962 (unpublished).
- [30] L. Silberstein, *Philos. Mag.* **33**, 521 (1917).
- [31] A. D. Buckingham and K. L. Clarke, *Chem. Phys. Lett.* **57**, 321 (1978).
- [32] R. A. Aziz and M. J. Slaman, *J. Chem. Phys.* **92**, 1030 (1990).
- [33] A *B* spline resembles the normal spline (interpolating scheme fitting a smooth curve via polynomials of a given degree) but it need not pass through all of the data points that are used in its definition. For additional information, see C. F. Gerald and P. O. Wheatley, in *Applied Numerical Analysis* (Addison-Wesley, Reading, MA, 1994).
- [34] L. Frommhold (private communication).
- [35] H. J. Achtermann, G. Magnus, and T. K. Bose, *J. Chem. Phys.* **94**, 5669 (1991).